An Unsplit Godunov Method for Ideal MHD via Constrained Transport in Three Dimensions

Thomas A. Gardiner [a] & James M. Stone [a,b]

[a]*Department of Astrophysical Sciences*
Princeton University
Princeton, NJ 08544

[b]*Program in Applied and Computational Mathematics*
Princeton University
Princeton, NJ 08544

Abstract

We present a single step, second-order accurate Godunov scheme for ideal MHD which is an extension of the method described in [1] to three dimensions. This algorithm combines the corner transport upwind (CTU) method of Colella for multidimensional integration, and the constrained transport (CT) algorithm for preserving the divergence-free constraint on the magnetic field. We describe the calculation of the PPM interface states for 3D ideal MHD which must include multidimensional "MHD source terms" and naturally respect the balance implicit in these terms by the $\nabla \cdot \mathbf{B} = 0$ condition. We compare two different forms for the CTU integration algorithm which require either 6- or 12-solutions of the Riemann problem per cell per time-step, and present a detailed description of the 6-solve algorithm. Finally, we present solutions for test problems to demonstrate the accuracy and robustness of the algorithm.

Key words:
PACS:

1 Introduction

In a previous paper [1] we described a two-dimensional, second-order accurate Godunov method for ideal MHD that evolves the magnetic field using the Constrained Transport (CT) [11] algorithm for preserving the divergence-free constraint on the magnetic field. In its simplest form, CT requires area-averaged values of the magnetic field which are stored at cell faces. We argued

that this is the most natural discrete representation of the field in that the integral form of the induction equation is based on area (rather than volume) averages, and therefore the discrete form of the equations should respect this difference. There are three important ingredients to our MHD algorithm: (1) a modification of the piecewise parabolic method (PPM) reconstruction step used to construct time-advanced estimates of the conserved variables on cell faces that are fed to the Riemann solver to incorporate multidimensional terms essential in MHD, (2) a new method for constructing the fluxes (at cell edges) of the area-averaged magnetic fields (at cell faces) from the fluxes returned by the Riemann solver (at cell faces) of volume averaged magnetic fields (at cell centers) which are based on the fundamental relationship between the area- and volume-averaged variables, and (3) a directionally unsplit integration algorithm based on the Corner Transport Upwind (CTU) method [7].

Through a series of test problems, we demonstrated the importance of each of the ingredients to our algorithm. In particular, we showed through tests based on the advection of two-dimensional field loops that our new methods for constructing the fluxes needed by the CT algorithm are essential for stability, and are an improvement over previous Godunov methods that use CT, e.g. [3]. We also showed that by using the second-order accurate CTU integration algorithm, a method could be constructed which has less numerical dissipation and has the important property of reducing exactly to the one-dimensional algorithm for plane-parallel, grid-aligned flows. Since CT does not require costly solutions to elliptic equations, we expect MHD Godunov schemes based on CT to be more cost effective that those that use divergence-cleaning [9,20]. Given the attractive properties of the method, it is of interest to extend it to three-dimensions for use in applications.

When directional splitting is used, the extension of Godunov methods from two- to three-dimensions is usually trivial. However, directional splitting is unsuitable for MHD, because it is impossible to enforce the divergence-free constraint between partial updates unless all three components of the magnetic field are updated together, which in turn violates the assumption basic to splitting that each dimensional operator is independent and can be split from the others. As a result, in [1] we adopted the unsplit CTU integration scheme. Even in hydrodynamics, the extension of CTU to three-dimensions is not trivial [18]. For our MHD algorithm, extension to three-dimensions requires modifying two of the three ingredients of the method, in particular (1) the PPM reconstruction algorithm must be modified to include multidimensional terms for MHD in such a way as to respect a *balance* law implied by the $\nabla \cdot \mathbf{B} = 0$ condition, and (2) the CTU algorithm must be modified to include source terms as well as the transverse flux gradient terms. The primary purpose of this paper is to describe in detail these modifications and to demonstrate that the resulting algorithm is both accurate and robust.

2

We extend our MHD test suite to three-dimensions to demonstrate the accuracy and fidelity of our method. We find that, once again, the passive advection of a multidimensional field loop is a challenging test of finite volume methods for MHD. In particular, for a field loop confined to the (x, y)-plane in three-dimensions advected with a constant velocity with $v_z \neq 0$, the vertical component of the magnetic field B_z will evolve unless care is made to ensure the multidimensional balance of MHD source terms in both the PPM characteristic tracing step and the transverse flux gradient update step. In fact, this observation leads to a useful definition of the appropriate difference stencil on which the divergence-free constraint must be maintained. If $\nabla \cdot \mathbf{B} = 0$ on a stencil which is different from that used to construct the fluxes of B_z, the latter will show unphysical evolution in this test for conservative algorithms. On the other hand, if a numerical method keeps B_z constant to round-off error on the test, it must preserve the divergence-free constraint on the appropriate stencil. Moreover, this test is another demonstration that it is *essential* to maintain the divergence-free constraint *exactly* in MHD, as was originally emphasized by [6]. This test, along with linear wave convergence tests, a test based on the propagation and convergence of nonlinear, circularly polarized Alfvén waves, and multidimensional blast wave tests are all presented in section 6.

The paper is organized as follows. In section 2, we write down the equations of ideal MHD solved by our method, and describe the finite-volume discretization of mass, momentum, and energy, and the finite-area discretization of the magnetic field. In section 3, we describe our extension of the PPM reconstruction algorithm to three-dimensional MHD. In section 4, we briefly review the upwind CT algorithms introduced in [1], while in section 5, we describe two formulations for the CTU integration algorithm to 3D. In section 6 we present the results of our test suite, while in section 7 we conclude.

2   Ideal Magnetohydrodynamics and Constrained Transport

The equations of ideal magnetohydrodynamics (MHD) can be written in conservative form as

$$\frac{\partial \rho}{\partial t} + \nabla \cdot (\rho \mathbf{v}) = 0 \tag{1}$$

$$\frac{\partial \rho \mathbf{v}}{\partial t} + \nabla \cdot (\rho \mathbf{v}\mathbf{v} - \mathbf{B}\mathbf{B}) + \nabla P^* = 0 \tag{2}$$

$$\frac{\partial \mathbf{B}}{\partial t} + \nabla \times (\mathbf{B} \times \mathbf{v}) = 0 \tag{3}$$

$$\frac{\partial E}{\partial t} + \nabla \cdot ((E + P^*)\mathbf{v} - \mathbf{B}(\mathbf{B} \cdot \mathbf{v})) = 0 \tag{4}$$

where ρ is the mass density, $\rho\mathbf{v}$ the momentum density, $\mathbf{B}$ the magnetic field, and E the total energy density. The total pressure $P^* \equiv P + (\mathbf{B} \cdot \mathbf{B})/2$ where P is the gas pressure. This system of equations is closed with the addition of an equation of state which relates the pressure and density to the internal energy,

$$\epsilon \equiv E - \rho(\mathbf{v} \cdot \mathbf{v})/2 - (\mathbf{B} \cdot \mathbf{B})/2 \ . \tag{5}$$

Throughout this paper we will assume an ideal gas equation of state for which $P = (\gamma - 1)\epsilon$, where γ is the ratio of specific heats. Note that we have chosen a system of units in which the magnetic permeability $\mu = 1$.

In addition to the evolutionary conservation laws, equations (1) through (4), the magnetic field must also obey the divergence free constraint, i.e. $\nabla \cdot \mathbf{B} = 0$. Here, as in [1], this is accomplished using the method of constrained transport (CT). In this method one starts from the differential form of the induction equation (4) and constructs an integral relation by area averaging the components of $\mathbf{B}$ normal to the grid cell faces over the respective face and applying Stoke's theorem. Analogous to the finite volume method, the resulting integral relation forms the basis of the numerical evolutionary equation. Note that one immediate consequence of CT is that the $\nabla \cdot \mathbf{B} = 0$ constraint on the magnetic field is satisfied in an integral sense over the smallest discretization scale, the grid cell. The volume averaged magnetic field components, which for example are necessary to calculate the internal energy, are defined equal to the average of the interface averaged components.

In this paper we will assume a regular, three dimensional, Cartesian grid. We will use the standard notation that grid cell (i, j, k) is centered at (x_i, y_j, z_k) and has a size $(\delta x, \delta y, \delta z)$. Time levels will be denoted by a superscript and interface values will be denoted by half increments to the index, $e.g.$ the volume averaged x-component of the magnetic field at time t^n is defined to be

$$B^n_{x,i,j,k} \equiv \frac{1}{2}\left(B^n_{x,i-1/2,j,k} + B^n_{x,i+1/2,j,k}\right) \ . \tag{6}$$

3 Calculating the Interface States

In this section we describe the calculation of the "interface states" in the PPM algorithm for ideal MHD in three dimensions. The PPM interface state algorithm is based upon the idea of dimensional splitting, and as a result is a one-dimensional algorithm including both spatial reconstruction and a characteristic evolution of the linearized system in primitive variables. For ideal MHD, however, it was shown in [1] that it is necessary to include multidi-

mensional terms when calculating the interface states. The three dimensional interface state algorithm is thus a generalization of the two-dimensional algorithm which for consistency must reduce to the two- and one-dimensional algorithm in the appropriate limits. The interface states in the PPM algorithm are typically calculated by evolving the system of equations in primitive variables. Consider the induction equation, which in component form is

$$\frac{\partial B_x}{\partial t} + \frac{\partial}{\partial y}\left(v_y B_x - B_y v_x\right) + \frac{\partial}{\partial z}\left(v_z B_x - B_z v_x\right) = 0 \tag{7}$$

$$\frac{\partial B_y}{\partial t} + \frac{\partial}{\partial x}\left(v_x B_y - B_x v_y\right) + \frac{\partial}{\partial z}\left(v_z B_y - B_z v_y\right) = 0 \tag{8}$$

$$\frac{\partial B_z}{\partial t} + \frac{\partial}{\partial x}\left(v_x B_z - B_x v_z\right) + \frac{\partial}{\partial y}\left(v_y B_z - B_y v_z\right) = 0 \ . \tag{9}$$

In these equations there are terms proportional to $\partial B_x/\partial x$, $\partial B_y/\partial y$ and $\partial B_z/\partial z$ which we will refer to as "MHD source terms". (When the system of equations for MHD is written in primitive variables, these source terms only appear in the induction equation. As a result we will not discuss the remaining MHD equations in this section.) The question before us is: which terms in the induction equation need to be included in the calculation of the interface states? In what follows we specialize to the calculation of the x-interface states; the y- and z-interface state calculation follows by symmetry.

3.1 2D MHD Interface State Algorithm

Before constructing the three-dimensional interface algorithm, it is instructive to recall the two-dimensional algorithm presented in [1]. For the two-dimensional (x, y)-case, the induction equation for B_z was simplified using the $\nabla \cdot \mathbf{B} = 0$ condition eliminating the MHD source terms from the evolutionary equation for B_z. The result is the following set of equations for calculating the x-interface states in 2D

$$\frac{\partial B_x}{\partial t} = 0 \tag{10}$$

$$\frac{\partial B_y}{\partial t} + \frac{\partial}{\partial x}\left(v_x B_y - B_x v_y\right) = 0 \tag{11}$$

$$\frac{\partial B_z}{\partial t} + \frac{\partial}{\partial x}\left(v_x B_z\right) - B_x\frac{\partial v_z}{\partial x} = 0 \ . \tag{12}$$

Utilizing the $\nabla \cdot \mathbf{B} = 0$ condition to eliminate the source terms from the evolutionary equation for B_z bestows a very important property on the calculation

5

of the interface states, namely the balance of the MHD source terms is exactly and explicitly included. The importance of this step can be easily understood by considering the advection of a magnetic field loop initially confined to the (x, y)-plane (*i.e.* $B_z = 0$) with $\mathbf{v} = $ constant, $v_z \neq 0$, and $\beta = 2P/B^2 \gg 1$. If the MHD source terms had not been eliminated from equation (9) prior to dimensional splitting and the following equation

$$\frac{\partial B_z}{\partial t} + \frac{\partial}{\partial x} \left(v_x B_z - B_x v_z \right) = 0 \tag{13}$$

was used instead of equation (12) the x-interface state would include an erroneous B_z evolution owing to the term $v_z \left(\partial B_x / \partial x \right)$. Experience shows that this error is not eliminated when updating the interface states due to transverse flux gradients in the CTU algorithm, leading to steady, secular growth of B_z which effectively warps the field loop. The important point to note here is that the *balance* of the MHD source terms resulting from the $\nabla \cdot \mathbf{B} = 0$ condition must be accurately represented in the calculation of the interface states.

3.2 3D MHD Interface State Algorithm

The 3D interface algorithm we construct is designed to explicitly incorporate the potential balance between the MHD source terms and to reduce exactly to the 2D interface states algorithm in the limit that the problems is two-dimensional and grid aligned. The essential idea is to rewrite the induction equation as follows prior to applying the idea of directional splitting.

$$\frac{\partial B_x}{\partial t} + \left\{ \frac{\partial}{\partial y} \left(v_y B_x - B_y v_x \right) - v_x \mathrm{L}_{xy} \left(\frac{\partial B_z}{\partial z} \right) \right\}$$
$$+ \left\{ \frac{\partial}{\partial z} \left(v_z B_x - B_z v_x \right) - v_x \mathrm{L}_{xz} \left(\frac{\partial B_y}{\partial y} \right) \right\} = 0 \tag{14}$$

$$\frac{\partial B_y}{\partial t} + \left\{ \frac{\partial}{\partial x} \left(v_x B_y - B_x v_y \right) - v_y \mathrm{L}_{yx} \left(\frac{\partial B_z}{\partial z} \right) \right\}$$
$$+ \left\{ \frac{\partial}{\partial z} \left(v_z B_y - B_z v_y \right) - v_y \mathrm{L}_{yz} \left(\frac{\partial B_x}{\partial x} \right) \right\} = 0 \tag{15}$$

$$\frac{\partial B_z}{\partial t} + \left\{ \frac{\partial}{\partial x} \left(v_x B_z - B_x v_z \right) - v_z \mathrm{L}_{zx} \left(\frac{\partial B_y}{\partial y} \right) \right\}$$

$$+\left\{\frac{\partial}{\partial y}\left(v_y B_z - B_y v_z\right) - v_z \mathrm{L}_{zy}\left(\frac{\partial B_x}{\partial x}\right)\right\} = 0 \ , \tag{16}$$

where we've added a limited amount of the transverse MHD source term to each component of the electric field gradient and grouped terms according to the fashion in which they will be split. The mathematical form of the limiter functions, e.g. L_{xy}, is determined by imposing constraints on the directionally split and unsplit system. Clearly, to recover the induction equation we have

$$\mathrm{L}_{xy}\left(\frac{\partial B_z}{\partial z}\right) = -\mathrm{L}_{xz}\left(\frac{\partial B_y}{\partial y}\right) \tag{17}$$

et cetra. Directionally split, we obtain the following system for the x-coordinate direction

$$\frac{\partial B_x}{\partial t} = 0 \tag{18}$$

$$\frac{\partial B_y}{\partial t} + \frac{\partial}{\partial x}\left(v_x B_y - B_x v_y\right) - v_y \mathrm{L}_{yx}\left(\frac{\partial B_z}{\partial z}\right) = 0 \tag{19}$$

$$\frac{\partial B_z}{\partial t} + \frac{\partial}{\partial x}\left(v_x B_z - B_x v_z\right) - v_z \mathrm{L}_{zx}\left(\frac{\partial B_y}{\partial y}\right) = 0 \ . \tag{20}$$

To determine the form of the limiter functions, we minimize the magnitude of the sum of the MHD source terms. For equation (20) we find

$$\mathrm{L}_{zx}\left(\frac{\partial B_y}{\partial y}\right) = \mathrm{minmod}\left(-\frac{\partial B_x}{\partial x}, \frac{\partial B_y}{\partial y}\right) \tag{21}$$

where the minmod function is defined as

$$\mathrm{minmod}\,(x, y) = \begin{cases} \mathrm{sign}(x)\min(|x|, |y|) & \text{if } xy > 0 \\ 0 & \text{otherwise.} \end{cases} \tag{22}$$

Note that this limiter function satisfies the constraint identified in equation (17). The mathematical form of the remaining limiter functions in equations (14 - 16) is given by cyclic permutation of (x, y, z) in equation (21) and application of the constraint noted in equation (17).

There is also a simple physical argument for why the limiter function takes the form described by equation (21). Considering equation (9), if $(\partial B_x/\partial x)$ and $(\partial B_y/\partial y)$ have opposite signs, but not necessarily the same magnitude

we wish to incorporate the balance of these two MHD source terms by adding and subtracting the term with the smaller magnitude so that the resulting (reduced) MHD source term is associated with only one of the flux gradients. If, on the other hand, these derivatives have the same sign, then there is no balance between the source terms and the induction equation should be unmodified. This is precisely the result of the minmod limited source term in equation (21).

Finally, we note that using the properties of the minmod function and the $\nabla \cdot \mathbf{B} = 0$ condition, equations (18-20) can be simplified to

$$\frac{\partial B_x}{\partial t} = 0 \tag{23}$$

$$\frac{\partial B_y}{\partial t} + \frac{\partial}{\partial x}\left(v_x B_y\right) - B_x \frac{\partial v_y}{\partial x} - v_y \text{minmod}\left(\frac{\partial B_x}{\partial x}, -\frac{\partial B_y}{\partial y}\right) = 0 \tag{24}$$

$$\frac{\partial B_z}{\partial t} + \frac{\partial}{\partial x}\left(v_x B_z\right) - B_x \frac{\partial v_z}{\partial x} - v_z \text{minmod}\left(\frac{\partial B_x}{\partial x}, -\frac{\partial B_z}{\partial z}\right) = 0 \tag{25}$$

for calculating the x-interface states. As a practical matter, these limited MHD source terms are evaluated in terms of the cell average of the magnetic field gradients, i.e. for equation (25) in cell (i, j, k) we use

$$\text{minmod}\left(\frac{B_{x,i+1/2,j,k} - B_{x,i-1/2,j,k}}{\delta x}, \frac{B_{z,i,j,k-1/2} - B_{x,i,j,k+1/2}}{\delta z}\right) \tag{26}$$

The equations for the y- and z-interface states follow from cyclic permutations of (x, y, z). In the limiting two dimensional case of either $\partial/\partial y = 0$ or $\partial/\partial z = 0$ this approach reduces to the interface state algorithm outlined in §3.1. Moreover, in the limiting two dimensional case of $\partial/\partial x = 0$, the x-interface state will equal the cell center state, just what one expects from one and two dimensional calculations. As a result, this algorithm for calculating the interface states preserves the $B_z = 0$ condition for the *gedanken* experiment described in §3.1 involving the advection of a magnetic field loop.

4   Constrained Transport (CT) Algorithm

The coupling of a Godunov, finite volume algorithm with the method of CT requires an algorithm for constructing the grid cell edge averaged electric fields (emfs) from the Godunov fluxes. This algorithm is typically referred to as a CT algorithm. The process of applying a CT algorithm to calculate the CT

emfs from the Godunov emf's can be described as a predictor / corrector process where the Godunov emf's are the predictor values and the resulting CT emfs are the corrector values. In [1] a simple framework for constructing CT algorithms was presented and a few CT algorithms were constructed and tested with the $\mathcal{E}^c$ CT algorithm selected as having the best properties. The $\mathcal{E}^c$ CT algorithm is constructed in such a way as contain an upwind bias (according to the contact mode) and to reduce to the correct Godunov emf for grid-aligned, plane-parallel flows. In this paper we will also use the $\mathcal{E}^c$ CT algorithm which for the sake of completeness we briefly review here.

Consider for the moment the calculation of the z-component of the electric field at the grid cell edge $(i+1/2, j+1/2, k)$. (The calculation of the x- and y-components of the CT electric fields follows an analogous procedure.) The CT algorithms described in [1] compute the CT electric field at this location from the four neighboring face center electric field components (Godunov fluxes) as well as estimates of the gradients of the electric field as follows

$$
\begin{aligned}
\mathcal{E}_{z,i+1/2,j+1/2,k} = \frac{1}{4} & \left(\mathcal{E}_{z,i+1/2,j,k} + \mathcal{E}_{z,i+1/2,j+1,k} + \mathcal{E}_{z,i,j+1/2,k} + \mathcal{E}_{z,i+1,j+1/2,k} \right) \\
& + \frac{\delta y}{8} \left(\left(\frac{\partial \mathcal{E}_z}{\partial y} \right)_{i+1/2,j+1/4,k} - \left(\frac{\partial \mathcal{E}_z}{\partial y} \right)_{i+1/2,j+3/4,k} \right) \\
& + \frac{\delta x}{8} \left(\left(\frac{\partial \mathcal{E}_z}{\partial x} \right)_{i+1/4,j+1/2,k} - \left(\frac{\partial \mathcal{E}_z}{\partial x} \right)_{i+3/4,j+1/2,k} \right) \, .
\end{aligned}
\tag{27}
$$

To complete this CT algorithm we need to specify a way to calculate the derivatives of $\mathcal{E}_z$ on the grid cell face. The $\mathcal{E}^c$ CT algorithm computes the electric field gradient at the grid cell face by selecting the "upwind" direction according to the contact mode, i.e.

$$
\left(\frac{\partial \mathcal{E}_z}{\partial y} \right)_{i+1/2,j+1/4,k} = \begin{cases} (\partial \mathcal{E}_z/\partial y)_{i,j+1/4,k} & \text{for } v_{x,i+1/2,j,k} > 0 \\ (\partial \mathcal{E}_z/\partial y)_{i+1,j+1/4,k} & \text{for } v_{x,i+1/2,j,k} < 0 \\ \frac{1}{2} \left((\partial \mathcal{E}_z/\partial y)_{i,j+1/4,k} + (\partial \mathcal{E}_z/\partial y)_{i+1,j+1/4,k} \right) & \text{otherwise} \end{cases}
\tag{28}
$$

with an analogous expression for the $(\partial \mathcal{E}_z/\partial x)$. The final detail involves the definition of the electric field derivatives in equation (28). These are computed using the face centered electric fields (Godunov fluxes) and a cell center "reference" value $\mathcal{E}^r_{z,i,j,k}$, e.g.

$$
\left(\frac{\partial \mathcal{E}_z}{\partial y} \right)_{i,j+1/4,k} = 2 \left(\frac{\mathcal{E}_{z,i,j+1/2,k} - \mathcal{E}^r_{z,i,j,k}}{\delta y} \right) \, .
\tag{29}
$$

9

In the 2D MHD CTU algorithm described in [1] and the 3D version described here, the cell center reference electric field $\mathcal{E}^r_{z,i,j,k}$ is computed using the cell center state at an appropriate time level. For the first interface flux calculation, using the interface states described in §3.2, the cell center reference electric field is computed using the cell center state $q^n_{i,j,k}$ when integrating from time t^n to t^{n+1}. The calculation of the cell center reference electric field in subsequent steps of the integration algorithm use time advanced states and will be described later in connection with the integration algorithm.

5   Corner Transport Upwind Algorithm

In this section we are interested in applying the CTU algorithm to the system of equations for ideal MHD. The CTU algorithm was originally described by Colella [7] as an unsplit, 2D finite volume algorithm for solving hyperbolic systems of conservation laws. The 3D generalization of the CTU algorithm was subsequently presented by Saltzman [18]. The CTU algorithm is generally set within a predictor-corrector formalism and utilizes PPM [8] when applied to Euler's equations - the archetypical system.

Prior to delving into the details of the numerical algorithms, it is worth while pointing out that the system of equations for ideal MHD differs from Euler's equations in non-trivial ways which are very important when applying the CTU algorithm to MHD. First, a straight forward application of the directional splitting technique to the MHD equations in primitive and conservative variables results in an incompatible set of equations. This results in the need to incorporate source terms in the transverse flux gradient corrections in the 2D and 3D CTU integration algorithm [1] since the PPM interface state algorithm uses the primitive variable form of the equations. Second, the treatment of the multidimensional MHD source terms in the MHD PPM interface states algorithm, described in §3, results in the need to incorporate source terms in the transverse flux gradient updates to the transverse components of the magnetic field at the interfaces. These details follow from the balance between multidimensional flux gradients imposed by the $\nabla \cdot \mathbf{B} = 0$ condition.

In this section we present two variants of the CTU integration algorithm. In §5.1 we present a brief, functional description of the 3D CTU algorithm as described by Saltzman [18] which we refer to here as the 12-solve algorithm since it requires 12 solutions to the Riemann problem per zone per time step. We will discuss the challenges associated with adapting this algorithm to the equations of ideal MHD. However, for a variety of reasons, the principle one being the complexity of the algorithm, we will not present the algorithmic elements for the 12-solve MHD CTU algorithm in detail. In §5.2 we present a simple variant on the CTU algorithm which requires only 6 solutions to the

Riemann problem per zone per time step and describe this 6-solve algorithm in detail. We summarize with a discussion of the strengths and weaknesses of this algorithm relative to the 12-solve CTU algorithm as a prelude to §6 where we present a variety of results comparing the 6-solve and 12-solve MHD CTU algorithms.

5.1 12-solve CTU

In this subsection we present a functional description of the 12-solve CTU algorithm as constructed for Euler's equations. This serves the goal of making the discussion more self-contained as well as allowing us to directly point out where particular elements of the integration algorithm pose challenges when applied to ideal MHD. For a more detailed description of the algorithm, or the theoretical underpinnings, see [7,15,18].

We begin by choosing a numerical flux function $\mathcal{F}(q_L, q_R)$ which is assumed to return a suitably accurate solution for the flux obtained by solving the Riemann problem associated with q_L and q_R, the left and right states. The 12-solve CTU algorithm can then be described as follows.

Step 1, calculate the left and right PPM interface states $q^*_{Lx,i+1/2,j,k}$, $q^*_{Rx,i+1/2,j,k}$, $q^*_{Ly,i,j+1/2,k}$, $q^*_{Ry,i,j+1/2,k}$, $q^*_{Lz,i,j,k+1/2}$ and $q^*_{Rz,i,j,k+1/2}$ and the associated interface fluxes

$$F^*_{x,i+1/2,j,k} = \mathcal{F}_x(q^*_{Lx,i+1/2,j,k}, q^*_{Rx,i+1/2,j,k}) \tag{30}$$

$$F^*_{y,i,j+1/2,k} = \mathcal{F}_y(q^*_{Ly,i,j+1/2,k}, q^*_{Ry,i,j+1/2,k}) \tag{31}$$

$$F^*_{z,i,j,k+1/2} = \mathcal{F}_z(q^*_{Lz,i,j,k+1/2}, q^*_{Rz,i,j,k+1/2}). \tag{32}$$

Step 2, for each interface state calculate two interface states evolved by $\delta t/3$ of a single transverse flux gradient, i.e.

$$q^{*|y}_{Lx,i+1/2,j,k} = q^*_{Lx,i+1/2,j,k} + \frac{\delta t}{3\delta y}\left(F^*_{y,i,j-1/2,k} - F^*_{y,i,j+1/2,k}\right) \tag{33}$$

$$q^{*|y}_{Rx,i+1/2,j,k} = q^*_{Rx,i+1/2,j,k} + \frac{\delta t}{3\delta y}\left(F^*_{y,i+1,j-1/2,k} - F^*_{y,i+1,j+1/2,k}\right) \tag{34}$$

$$q^{*|z}_{Lx,i+1/2,j,k} = q^*_{Lx,i+1/2,j,k} + \frac{\delta t}{3\delta z}\left(F^*_{z,i,j,k-1/2} - F^*_{z,i,j,k+1/2}\right) \tag{35}$$

$$q^{*|z}_{Rx,i+1/2,j,k} = q^*_{Rx,i+1/2,j,k} + \frac{\delta t}{3\delta z}\left(F^*_{z,i+1,j,k-1/2} - F^*_{z,i+1,j,k+1/2}\right) \tag{36}$$

with y- and z-interface states being defined in an equivalent manner by cyclic

11

permutation of (x, y, z) and (i, j, k). For each of the $\delta t/3$ updated interface states, calculate the associated flux, giving the two x-interface fluxes

$$F_{x,i+1/2,j,k}^{*|y} = \mathcal{F}_x(q_{Lx,i+1/2,j,k}^{*|y}, q_{Rx,i+1/2,j,k}^{*|y}) \tag{37}$$

$$F_{x,i+1/2,j,k}^{*|z} = \mathcal{F}_x(q_{Lx,i+1/2,j,k}^{*|z}, q_{Rx,i+1/2,j,k}^{*|z}) \tag{38}$$

and similar expressions for the y- and z-interface fluxes.

Step 3, at each interface evolve the PPM interface states by $\delta t/2$ of the transverse flux gradients, i.e.

$$q_{Lx,i+1/2,j,k}^{n+1/2} = q_{Lx,i+1/2,j,k}^{*} + \frac{\delta t}{2\delta y}\left(F_{y,i,j-1/2,k}^{*|z} - F_{y,i,j+1/2,k}^{*|z}\right) \tag{39}$$

$$+ \frac{\delta t}{2\delta z}\left(F_{z,i,j,k-1/2}^{*|y} - F_{z,i,j,k+1/2}^{*|y}\right) \tag{40}$$

$$q_{Rx,i+1/2,j,k}^{n+1/2} = q_{Rx,i+1/2,j,k}^{*} + \frac{\delta t}{2\delta y}\left(F_{y,i+1,j-1/2,k}^{*|z} - F_{y,i+1,j+1/2,k}^{*|z}\right) \tag{41}$$

$$+ \frac{\delta t}{2\delta z}\left(F_{z,i+1,j,k-1/2}^{*|y} - F_{z,i+1,j,k+1/2}^{*|y}\right) \tag{42}$$

with y- and z-interface states being defined in an equivalent manner by cyclic permutation of (x, y, z) and (i, j, k). For each of the $\delta t/2$ updated interface states, calculate the associated flux, giving the x-interface flux

$$F_{x,i+1/2,j,k}^{n+1/2} = \mathcal{F}_x(q_{Lx,i+1/2,j,k}^{n+1/2}, q_{Rx,i+1/2,j,k}^{n+1/2}) \tag{43}$$

and similar expressions for the y- and z-interface fluxes.

Step 4, update the the conserved variables from time n to $n+1$ via the fully corner coupled numerical fluxes

$$q_{i,j,k}^{n+1} = q_{i,j,k}^{n} + \frac{\delta t}{\delta x}\left(F_{x,i-1/2,j,k}^{n+1/2} - F_{x,i+1/2,j,k}^{n+1/2}\right) \tag{44}$$

$$+ \frac{\delta t}{\delta y}\left(F_{y,i,j-1/2,k}^{n+1/2} - F_{y,i,j+1/2,k}^{n+1/2}\right) + \frac{\delta t}{\delta z}\left(F_{z,i,j,k-1/2}^{n+1/2} - F_{z,i,j,k+1/2}^{n+1/2}\right). \tag{45}$$

This completes the description of the 12-solve CTU algorithm for a typical system of conservation laws, such as Euler's equations. Unfortunately, as written above, the 12-solve CTU algorithm does not result in a useful method for ideal MHD. This can be understood on rather general grounds by noting that the intermediate steps in the algorithm use partial updates based on a dimensional splitting of the equations in conservation form. This in turn ignores the potential balance between flux gradients in different directions (in particular MHD

source terms associated with those flux gradients) which is always present for MHD owing to the $\nabla \cdot \mathbf{B} = 0$ constraint. We make this point more concrete by considering two points in detail.

First, note that the parallel flux gradient terms (x-flux gradient at x-interfaces, etc.) are included in the PPM interface states algorithm using the dimensionally split, primitive form of the equations for MHD. Meanwhile, the transverse flux gradient terms are included using the conservative form of the equations. Since the dimensionally split primitive and conservative form of the equations for MHD are not commensurate, this amounts to neglecting certain MHD source terms resulting in a formally first order accurate integration algorithm. In addition, such an algorithm would also show secular evolution of a magnetic field component perpendicular to the magnetic field loop in the *gedanken* experiment discussed in §3. Note that the same is true of the two-dimensional CTU algorithm [1], which required the addition of source terms to the transverse flux gradient correction step. For the 3D 12-solve CTU algorithm, with two predictor steps, this source term correction procedure is increasingly complicated.

To see why this is so, consider step 2 in the description of the 12-solve CTU algorithm just presented. In particular, note that in this step one generates two interface states at each interface, by evolving the PPM interface state by $\delta t/3$ of one transverse flux gradient. In other words, for each interface normal component of the magnetic field (used to define the divergence of the magnetic field), one generates two normal components, each of which is evolved by one half of a CT or Stokes EMF field loop. (As an aside, note that at this stage $\nabla \cdot \mathbf{B} = 0$ is satisfied in the sense of the average of these normal magnetic field components.) It is useful at this stage to consider again the *gedanken* experiment discussed in §3 and consider the generation of the two z-interface states in step 2 of the integration algorithm. As a result of the MHD source terms in the x- and y-flux gradients, namely $v_z \left(\partial B_x / \partial x \right)$ and $v_z \left(\partial B_y / \partial y \right)$, these two z-interface states will show a non-zero, in fact equal and opposite, evolution of B_z. This is a manifestation of a failure to satisfy the balance condition discussed in §3. Thus what we find is that it is the balanced, dimensionally split system presented in §3, equations (14)-(16), which should replace the straight forward dimensionally split conservative form of the induction equation in steps 2 and 3 of the 12-solve CTU algorithm. In practice, this means that the interface *normal* components of the magnetic field must incorporate a source term so as to maintain this balance, and the two, say z-interface states, which are generated must use the same source term, with opposite sign, so as to maintain the magnetic divergence condition in an average sense. Finally, note that as a result of dimensionally splitting the system, the momentum and energy update in step 2 and 3 also require the addition of source terms to balance terms like $B_x \left(\partial B_x / \partial x \right)$ and $\mathbf{B} \cdot \mathbf{v} \left(\partial B_x / \partial x \right)$ etc.

The net result is that a well balanced, 12-solve CTU algorithm for ideal MHD can be constructed by using partial updates based on a dimensional splitting of the MHD equations using a carefully chosen, non-conservative form for the intermediate steps. This form is found by paying particular attention to the implicit balance between the flux gradients, as was done for the induction equation in §3 for the PPM interface state algorithm. The advantage of this approach is a computational algorithm which is optimally stable for CFL numbers ≤ 1. The disadvantage is that the algorithm is complicated. We have implemented the 12-solve MHD CTU algorithm as described above and present results of tests of the method in §6. However, the complexity of the method motivates us to find a simpler alternative, which we describe below.

5.2   6-solve CTU variant for MHD

In this subsection we present a simple variant on the 12-solve CTU algorithm which we will henceforth refer to as the 6-solve algorithm. For Euler's equations, the 6-solve algorithm can be described concisely as the 12-solve CTU algorithm of §5.1 omitting step 2 and replacing $F^{*|y}_{x,i+1/2,j,k}$ and $F^{*|z}_{x,i+1/2,j,k}$ with $F^*_{x,i+1/2,j,k}$ (and similarly for the y- and z-fluxes) in step 3. Alternatively, one may also describe it as a formal extension of the 2D CTU algorithm in which the parallel and transverse flux gradients are included in the interface states in a two-step process. In what follows we present a functional description of this 6-solve CTU algorithm for MHD including a detailed description of the treatment of the MHD source terms and constrained transport electric fields.

Step 1, calculate the left and right PPM interface states $q^*_{Lx,i+1/2,j,k}$, $q^*_{Rx,i+1/2,j,k}$, $q^*_{Ly,i,j+1/2,k}$, $q^*_{Ry,i,j+1/2,k}$, $q^*_{Lz,i,j,k+1/2}$ and $q^*_{Rz,i,j,k+1/2}$ including the MHD source terms described in §3.2 and the associated interface fluxes

$$F^*_{x,i+1/2,j,k} = \mathcal{F}_x(q^*_{Lx,i+1/2,j,k}, q^*_{Rx,i+1/2,j,k}) \tag{46}$$

$$F^*_{y,i,j+1/2,k} = \mathcal{F}_y(q^*_{Ly,i,j+1/2,k}, q^*_{Ry,i,j+1/2,k}) \tag{47}$$

$$F^*_{z,i,j,k+1/2} = \mathcal{F}_z(q^*_{Lz,i,j,k+1/2}, q^*_{Rz,i,j,k+1/2}). \tag{48}$$

Step 2, apply the CT algorithm of §4 to calculate the CT electric fields $\mathcal{E}^*_{x,i,j+1/2,k+1/2}$, $\mathcal{E}^*_{y,i+1/2,j,k+1/2}$ and $\mathcal{E}^*_{z,i+1/2,j+1/2,k}$ using the numerical fluxes from step 1 and a cell center reference electric field calculated using the initial data at time level n, i.e. $q^n_{i,j,k}$.

Step 3, at each interface evolve the PPM interface states by $\delta t/2$ of the transverse flux gradients. The hydrodynamic variables (mass, momentum and energy density) are advanced using

$$q_{Lx,i+1/2,j,k}^{n+1/2} = q_{Lx,i+1/2,j,k}^{*} + \frac{\delta t}{2\delta y}\left(F_{y,i,j-1/2,k}^{*} - F_{y,i,j+1/2,k}^{*}\right)$$

$$+\frac{\delta t}{2\delta z}\left(F_{z,i,j,k-1/2}^{*} - F_{z,i,j,k+1/2}^{*}\right) + \frac{\delta t}{2}S_{x,i,j,k} \tag{49}$$

$$q_{Rx,i+1/2,j,k}^{n+1/2} = q_{Rx,i+1/2,j,k}^{*} + \frac{\delta t}{2\delta y}\left(F_{y,i+1,j-1/2,k}^{*} - F_{y,i+1,j+1/2,k}^{*}\right)$$

$$+\frac{\delta t}{2\delta z}\left(F_{z,i+1,j,k-1/2}^{*} - F_{z,i+1,j,k+1/2}^{*}\right) + \frac{\delta t}{2}S_{x,i+1,j,k} \tag{50}$$

where the x-interface MHD source term for the momentum density

$$(S_{x,i,j,k})_{\rho\mathbf{v}} = \mathbf{B}_{i,j,k}\left(\frac{\partial B_x}{\partial x}\right)_{i,j,k} \tag{51}$$

and the energy density

$$(S_{x,i,j,k})_E = (B_y v_y)_{i,j,k}\text{minmod}\left(-\frac{\partial B_z}{\partial z}, \frac{\partial B_x}{\partial x}\right)_{i,j,k} +$$

$$(B_z v_z)_{i,j,k}\text{minmod}\left(-\frac{\partial B_y}{\partial y}, \frac{\partial B_x}{\partial x}\right)_{i,j,k}. \tag{52}$$

The magnetic field components are evolved using the CT electric fields in place of the predictor fluxes. The interface normal component of the magnetic field is evolved using the integral form of the Stokes loop,

$$B_{x,i+1/2,j,k}^{n+1/2} = B_{x,i+1/2,j,k}^{n} - \frac{\delta t}{2\delta y}\left(\mathcal{E}_{z,i+1/2,j+1/2,k}^{*} - \mathcal{E}_{z,i+1/2,j-1/2,k}^{*}\right)$$

$$+\frac{\delta t}{2\delta z}\left(\mathcal{E}_{y,i+1/2,j,k+1/2}^{*} - \mathcal{E}_{y,i+1/2,j,k-1/2}^{*}\right). \tag{53}$$

The y-component of the magnetic field is evolved using

$$(B_y)_{Lx,i+1/2,j,k}^{n+1/2} = (B_y)_{Lx,i+1/2,j,k}^{*} - \frac{\delta t}{4\delta z}\left(\mathcal{E}_{x,i,j+1/2,k+1/2}^{*} - \mathcal{E}_{x,i,j+1/2,k-1/2}^{*}\right)$$

$$-\frac{\delta t}{4\delta z}\left(\mathcal{E}_{x,i,j-1/2,k+1/2}^{*} - \mathcal{E}_{x,i,j-1/2,k-1/2}^{*}\right)$$

$$+\frac{\delta t}{2}(S_{x,i,j,k})_{B_y} \tag{54}$$

$$(B_y)_{Rx,i+1/2,j,k}^{n+1/2} = (B_y)_{Rx,i+1/2,j,k}^{*} - \frac{\delta t}{4\delta z}\left(\mathcal{E}_{x,i+1,j+1/2,k+1/2}^{*} - \mathcal{E}_{x,i+1,j+1/2,k-1/2}^{*}\right)$$

$$-\frac{\delta t}{4\delta z}\left(\mathcal{E}_{x,i+1,j-1/2,k+1/2}^{*} - \mathcal{E}_{x,i+1,j-1/2,k-1/2}^{*}\right)$$

$$+\frac{\delta t}{2}(S_{x,i+1,j,k})_{B_y} \tag{55}$$

with

$$(S_{x,i,j,k})_{B_y} = (v_y)_{i,j,k}\text{minmod}\left(-\frac{\partial B_z}{\partial z}, \frac{\partial B_x}{\partial x}\right)_{i,j,k}. \tag{56}$$

The z-component of the magnetic field is evolved using

$$(B_z)_{Lx,i+1/2,j,k}^{n+1/2} = (B_z)_{Lx,i+1/2,j,k}^* + \frac{\delta t}{4\delta y}\left(\mathcal{E}_{x,i,j+1/2,k+1/2}^* - \mathcal{E}_{x,i,j-1/2,k+1/2}^*\right)$$

$$+\frac{\delta t}{4\delta y}\left(\mathcal{E}_{x,i,j+1/2,k-1/2}^* - \mathcal{E}_{x,i,j-1/2,k-1/2}^*\right)$$

$$+\frac{\delta t}{2}(S_{x,i,j,k})_{B_z} \tag{57}$$

$$(B_z)_{Rx,i+1/2,j,k}^{n+1/2} = (B_z)_{Rx,i+1/2,j,k}^* + \frac{\delta t}{4\delta y}\left(\mathcal{E}_{x,i+1,j+1/2,k+1/2}^* - \mathcal{E}_{x,i+1,j-1/2,k+1/2}^*\right)$$

$$+\frac{\delta t}{4\delta y}\left(\mathcal{E}_{x,i+1,j+1/2,k-1/2}^* - \mathcal{E}_{x,i+1,j-1/2,k-1/2}^*\right)$$

$$+\frac{\delta t}{2}(S_{x,i+1,j,k})_{B_z} \tag{58}$$

with

$$(S_{x,i,j,k})_{B_z} = (v_z)_{i,j,k}\text{minmod}\left(-\frac{\partial B_y}{\partial y}, \frac{\partial B_x}{\partial x}\right)_{i,j,k}. \tag{59}$$

Note that the origin of these MHD source terms for the transverse components of the magnetic field can be clearly seen as resulting from the directional splitting of the induction equation described in §3.2. The momentum and energy density MHD source terms originate from the use of the primitive variable form of the MHD equations to calculate the PPM interface states. The y- and z-interface states are advanced in an equivalent manner by cyclic permutation of (x, y, z) and (i, j, k) in the above expressions.

Step 4, for each of the $\delta t/2$ updated interface states, calculate the associated flux, giving the x-interface flux

$$F_{x,i+1/2,j,k}^{n+1/2} = \mathcal{F}_x(q_{Lx,i+1/2,j,k}^{n+1/2}, q_{Rx,i+1/2,j,k}^{n+1/2}) \tag{60}$$

and similar expressions for the y- and z-interface fluxes.

Step 5, apply the CT algorithm of §4 to calculate the CT electric fields $\mathcal{E}_{x,i,j+1/2,k+1/2}^{n+1/2}$, $\mathcal{E}_{y,i+1/2,j,k+1/2}^{n+1/2}$ and $\mathcal{E}_{z,i+1/2,j+1/2,k}^{n+1/2}$ using the numerical fluxes from step 4 and a cell center reference electric field calculated using the cell average state at time level $n + 1/2$ which is calculated as follows. The cell center

16

magnetic field components are defined as equaling the arithmetic average of the interface magnetic field components, $B_{x,i,j,k}^{n+1/2} = (B_{x,i+1/2,j,k}^{n+1/2} + B_{x,i-1/2,j,k}^{n+1/2})/2$ and similarly for the y- and z-components. The mass and momentum density are computed using a conservative update with the predictor fluxes from step 1,

$$q_{i,j,k}^{n+1/2} = q_{i,j,k}^n + \frac{\delta t}{2\delta x}\left(F_{x,i-1/2,j,k}^* - F_{x,i+1/2,j,k}^*\right) \tag{61}$$
$$+ \frac{\delta t}{2\delta y}\left(F_{y,i,j-1/2,k}^* - F_{y,i,j+1/2,k}^*\right) + \frac{\delta t}{2\delta z}\left(F_{z,i,j,k-1/2}^* - F_{z,i,j,k+1/2}^*\right) \ .$$

Step 6, update the solution from time level n to $n+1$. The hydrodynamic variables (mass, momentum and energy density) are advanced using the standard the flux integral relation,

$$q_{i,j,k}^{n+1} = q_{i,j,k}^n + \frac{\delta t}{\delta x}\left(F_{x,i-1/2,j,k}^{n+1/2} - F_{x,i+1/2,j,k}^{n+1/2}\right) \tag{62}$$
$$+ \frac{\delta t}{\delta y}\left(F_{y,i,j-1/2,k}^{n+1/2} - F_{y,i,j+1/2,k}^{n+1/2}\right) + \frac{\delta t}{\delta z}\left(F_{z,i,j,k-1/2}^{n+1/2} - F_{z,i,j,k+1/2}^{n+1/2}\right)$$

and the interface averaged normal components of the magnetic field are advanced using a Stokes loop integral,

$$B_{x,i+1/2,j,k}^{n+1} = B_{x,i+1/2,j,k}^n - \frac{\delta t}{\delta y}\left(\mathcal{E}_{z,i+1/2,j+1/2,k}^{n+1/2} - \mathcal{E}_{z,i+1/2,j-1/2,k}^{n+1/2}\right)$$
$$+ \frac{\delta t}{\delta z}\left(\mathcal{E}_{y,i+1/2,j,k+1/2}^{n+1/2} - \mathcal{E}_{y,i+1/2,j,k-1/2}^{n+1/2}\right) \ , \tag{63}$$

$$B_{y,i,j+1/2,k}^{n+1} = B_{y,i,j+1/2,k}^n + \frac{\delta t}{\delta x}\left(\mathcal{E}_{z,i+1/2,j+1/2,k}^{n+1/2} - \mathcal{E}_{z,i-1/2,j+1/2,k}^{n+1/2}\right)$$
$$- \frac{\delta t}{\delta z}\left(\mathcal{E}_{x,i,j+1/2,k+1/2}^{n+1/2} - \mathcal{E}_{x,i,j+1/2,k-1/2}^{n+1/2}\right) \ , \tag{64}$$

and

$$B_{z,i,j,k+1/2}^{n+1} = B_{z,i,j,k+1/2}^n - \frac{\delta t}{\delta x}\left(\mathcal{E}_{y,i+1/2,j,k+1/2}^{n+1/2} - \mathcal{E}_{y,i-1/2,j,k+1/2}^{n+1/2}\right)$$
$$+ \frac{\delta t}{\delta y}\left(\mathcal{E}_{x,i,j+1/2,k+1/2}^{n+1/2} - \mathcal{E}_{x,i,j-1/2,k+1/2}^{n+1/2}\right) \ . \tag{65}$$

This completes the description of the 6-solve CTU algorithm. This relatively simple 3D integration algorithm is second order accurate and has the advan-

tage over the 12-solve CTU algorithm that no source terms need be included in the evolution of the interface normal components of the magnetic field. This algorithm is designed in such a way that for grid aligned flows it reduces exactly to the 2D CTU and 1D PPM integration algorithms for problems involving the relevant symmetry. Additionally, consideration of the field loop advection *gedanken* experiment described in §3 shows that the 6-solve CTU algorithm is well balanced and preserves the $B_z = 0$ condition exactly. The downside of the present 6-solve algorithm is that we observe experimentally that the algorithm is stable for CFL $< 1/2$. When compared to the 12-solve algorithm, this is compensated by the fact that it requires half as many Riemann solutions per time step. Hence, to a large extent the 6-solve and 12-solve algorithms show similar computational cost: two time-steps with the 6-solve algorithm at a CFL number of $1/2$ is nearly equivalent to one time-step with the 12-solve algorithm with a CFL number of one.

6 Tests

In this section we present results obtained with the 6-solve CTU + CT integration algorithm just described. For the sake of comparison, and clarification of the dominant differences between the results obtained with the 6-solve and 12-solve algorithms, some results using the 12-solve algorithm will also be included. We will find in this section, through a series of tests, that the dominant difference between the two are the stability domain. Otherwise, they are quite comparable in accuracy and computational cost. As a result, in practical applications we prefer the 6-solve algorithm for MHD on account of its simplicity and smaller memory footprint.

6.1 Field Loop Advection

In this section we discuss and present results for the advection of a magnetic field loop. In order to narrow the focus and clarify the discussion, in this section we will concern ourselves primarily with the the initial conditions in which the density ρ, velocity $\mathbf{v}$, and pressure P are constants, and the magnetic field is weak in the sense that $\beta = 2P/B^2 \gg 1$. In this limit, the evolution equations for the magnetic field are well approximated by the advection of a set of passive scalar functions, say the components of the magnetic vector potential. In the construction of the 2D CTU-CT algorithm [1] as well as the 3D 6-solve and 12-solve algorithms presented here we have found that recovering the correct solution in this limiting case can be surprisingly difficult for conservative, finite volume algorithms applied to the ideal MHD equations.

As a concrete example of a situation in which this problem can be challenging, consider the field loop advection test problem studied in [1] and discussed as a *gedanken* experiment in §3. Specifically, consider a field loop confined to the (x, y)-plane, i.e. $B_z = 0$, and a constant advection velocity field with $v_z \neq 0$. If care is not taken to respect the balance between the MHD source terms in calculating the interface states, updating them with transverse flux gradients, etc. one can find an erroneous and sometimes *secular* evolution of B_z. It should be noted that these concerns are not limited to CTU or PPM which use a predictor step. For example schemes with are conservative but do not satisfy $\nabla \cdot \mathbf{B} = 0$ will also find erroneous evolution for B_z in this problem. There is an interesting corollary which results from this observation. If a conservative numerical algorithm can solve this magnetic field loop advection problem and preserve the solution $B_z = 0$ for all time, it also satisfies the $\nabla \cdot \mathbf{B} = 0$ condition.

We begin by selecting a computational domain $-0.5 \leq x \leq 0.5$, $-0.5 \leq y \leq 0.5$, and $-1 \leq z \leq 1$, resolved on a $N \times N \times 2N$ grid and apply periodic boundary conditions. The hydrodynamical state is uniform with a density $\rho = 1$, pressure $P = 1$, and velocity components $(v_x, v_y, v_z) = (1, 1, 2)$. The initialization of the magnetic field is most easily described in terms of a vector potential in the coordinate system (x_1, x_2, x_3) which is related to the computational coordinate system (x, y, z) via the rotation

$$
\begin{aligned}
x_1 &= (2x + z)/\sqrt{5} \\
x_2 &= y \\
x_3 &= (-x + 2z)/\sqrt{5} \, .
\end{aligned}
\tag{66}
$$

In particular, we choose $A_1 = A_2 = 0$ and

$$
A_3 = \begin{cases} B_0(R - r) & \text{for } r \leq R \\ 0 & \text{for } r > R \end{cases}
\tag{67}
$$

where $B_0 = 10^{-3}$, $R = 0.3$ and $r = \sqrt{x_1^2 + x_2^2}$ in the domain $-0.5\lambda_1 \leq x_1 \leq 0.5\lambda_1$, $-0.5\lambda_2 \leq x_2 \leq 0.5\lambda_2$. To satisfy the periodic boundary conditions we choose $\lambda_1 = 2/\sqrt{5}$ and $\lambda_2 = 1$ and define $A_3(x_1 + n\lambda_1, x_2 + m\lambda_2, x_3) = A_3(x_1, x_2, x_3)$ for all integers (n, m).

As a quantitative measure of the dissipation in the algorithm we plot the time evolution of the volume averaged magnetic energy density $< B^2 >$ normalized to the initial (analytic) value $< B^2 >= (\sqrt{5}\pi R^2/2)B_0^2$ in Figure 1. Interestingly, the magnetic energy density $< B^2 >$ shows a temporal evolution similar to what was observed with the 2D algorithm in [1]. Namely, it can be well fit as a power law of the form $< B^2 >= C(1 - (t/\tau)^\alpha)$ where

$\tau = (3.22 \times 10^2, \ 3.68 \times 10^3, \ 2.65 \times 10^4)$ and $\alpha = (0.365, \ 0.328, \ 0.320)$ for $N = (32, \ 64, \ 128)$ respectively. Moreover, these values are quite comparable to the time constant $\tau = 1.061 \times 10^4$ and exponent $\alpha = 0.291$ found in the 2D calculation.

For the specific case of a cylindrical magnetic field loop with translation invariance in the z-direction ($\partial/\partial z = 0$) the 6-solve and 12-solve algorithms studied in this paper reduce exactly to the 2D algorithm presented in [1]. As such, the 3D algorithms presented here give the same solution as the 2D algorithm in [1] and preserve the solution $B_z = 0$ for all time (we have explicitly tested that this is true with our implementation of the method). With the axis of the cylindrical field loop is aligned along a non-special direction with respect to the grid, preserving this property is non-trivial.

As a quantitative measure of the ability of the algorithm to preserve $B_3 = 0$ we plot the normalized error $< |B_3| > /B_0$ in Figure 1. This error is calculated by contracting the cell center magnetic field with a unit vector in the x_3-direction and computing the volume average of its absolute value. From this plot it is clear that the convergence rate of $< |B_3| > /B_0$ as measured in either the initial conditions, or the solution at time $= 1$ is approximately first order. This behavior is consistent with the observation that the 3-component of the magnetic energy is dominant on the axis and at the boundary of the magnetic cylinder where the current density is initially singular, as shown in figure 2. It is also worth noting that away from these regions, the solution preserves the 3-component of the magnetic energy quite small. This would not be the case if care were not taken to balance the MHD source terms in the integration algorithm.
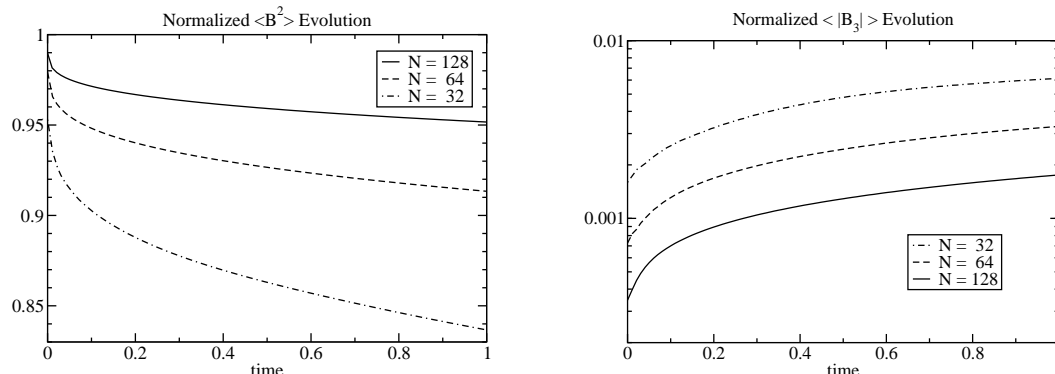

Fig. 1. Time evolution of the normalized, volume average magnetic energy density $< B^2 >$ and the component along the x_3-direction, $< B_3^2 >$, for three different grid resolutions using the 6-solve integration algorithm.

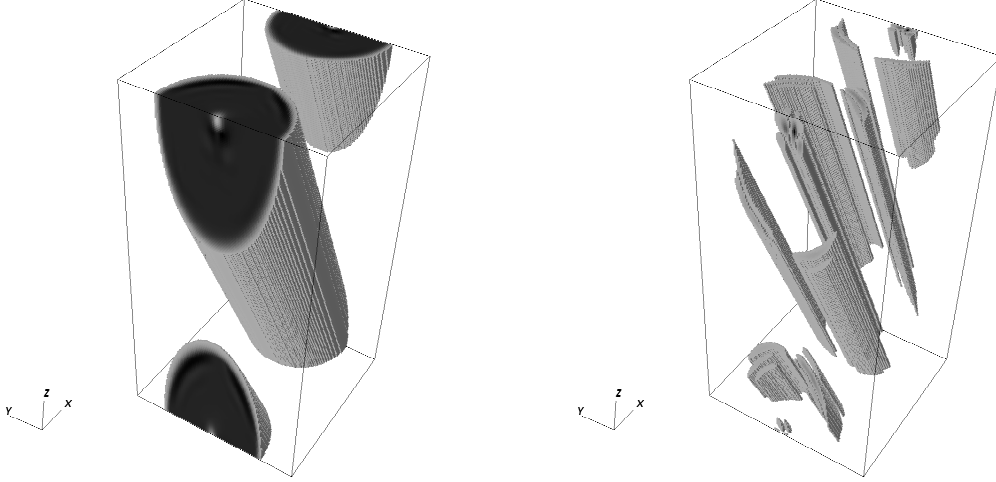Fig. 2. Thresholded image of the magnetic energy (*left*) and the 3-component of the magnetic energy, $B_3^2/2$, at time = 1.

6.2   Linear Wave Convergence

In this subsection we present the results of a convergence study for both the 6-solve and 12-solve CTU-CT MHD algorithms. The problem we study is the propagation of linear amplitude, planar waves in a direction which is oblique to the grid. The physical conditions of the problem are most easily described in a coordinate system $(x_1,\ x_2,\ x_3)$ which is chosen such that the wave propagates parallel to the x_1-axis. In this coordinate system, the initial conserved variable state vector is given by

$$q^0 = \bar{q} + \varepsilon R_p \cos\left(\frac{2\pi x_1}{\lambda}\right) \tag{68}$$

where $\bar{q}$ is the mean background state, $\varepsilon = 10^{-6}$ is the wave amplitude, and R_p is the right eigenvector in conserved variables for wave mode p (calculated in the state $\bar{q}$). In order to enable others to perform the same tests presented here and compare the results in a quantitative manner, we include the numerical values for the right eigenvectors in the appendix.

The mean background state $\bar{q}$ is selected so that the wave speeds are well separated and there are no inherent symmetries in the magnetic field orientation (when initialized on the grid). The density $\bar{\rho} = 1$ and gas pressure $\bar{P} = 1/\gamma = 3/5$. The velocity component $\bar{v}_1 = 1$ for the entropy mode test and $\bar{v}_1 = 0$ for all other wave modes. The transverse velocity components $\bar{v}_2 = \bar{v}_3 = 0$. The magnetic field components $\bar{B}_1 = 1$, $\bar{B}_2 = 3/2$, and $\bar{B}_3 = 0$. With this choice, the slow mode speed $c_s = 1/2$, the Alfvén speed $c_a = 1$, and the fast mode speed $c_f = 2$ in the x_1-direction.

21

The computational domain extends from $0 \leq x \leq 3.0$, $0 \leq y \leq 1.5$, and $0 \leq z \leq 1.5$, is resolved on a $2N \times N \times N$ grid and uses periodic boundary conditions. Initializing this problem on the computational grid is accomplished by applying a coordinate transformation

$$
\begin{aligned}
x &= x_1 \cos\alpha \cos\beta - x_2 \sin\beta - x_3 \sin\alpha \cos\beta \\
y &= x_1 \cos\alpha \sin\beta + x_2 \cos\beta - x_3 \sin\alpha \sin\beta \\
z &= x_1 \sin\alpha + x_3 \cos\alpha
\end{aligned}
\tag{69}
$$

from the (x_1, x_2, x_3) coordinate system to the (x, y, z) coordinate system of the grid with $\sin\alpha = 2/3$ and $\sin\beta = 2/\sqrt{5}$. With this choice, there is one wave period along each grid direction and the wavelength $\lambda = 1$. The interface components of the magnetic field are initialized via a magnetic vector potential so as to ensure $\nabla \cdot \mathbf{B} = 0$.

The error in the solution is calculated after propagating the wave for a distance equal to one wavelength. Hence, the initial state is evolved for a time $t = \lambda/c$ where c is the speed of the wave mode under consideration. For each component s of the conserved variable vector q we calculate the L1-error with respect to the initial conditions

$$
\delta q_s = \frac{1}{2N^3} \sum_{i,j,k} |q_{i,j,k,s}^n - q_{i,j,k,s}^0|
\tag{70}
$$

by summing over all grid cells (i, j, k). We use the cell center components of the magnetic field in computing this error. In figure 3 we plot the norm of this error vector

$$
\|\delta q\| = \sqrt{\sum_s (\delta q_s)^2}
\tag{71}
$$

for the fast, Alfvén, slow and entropy modes. Both algorithms demonstrate a second order convergence. With the exception of the slow mode, the 6-solve algorithm shows lower errors than the 12-solve algorithm. Note that the choice of maximum resolution in the convergence study for each algorithm and wave mode was selected on the basis of the "cost" of the computation.

6.3   Circularly Polarized Alfvén Wave

In this section we present results for the propagation of a circularly polarized Alfvén wave in a periodic domain using both the 6-solve and 12-solve algorithms. This problem is interesting from the perspective that the wave is an
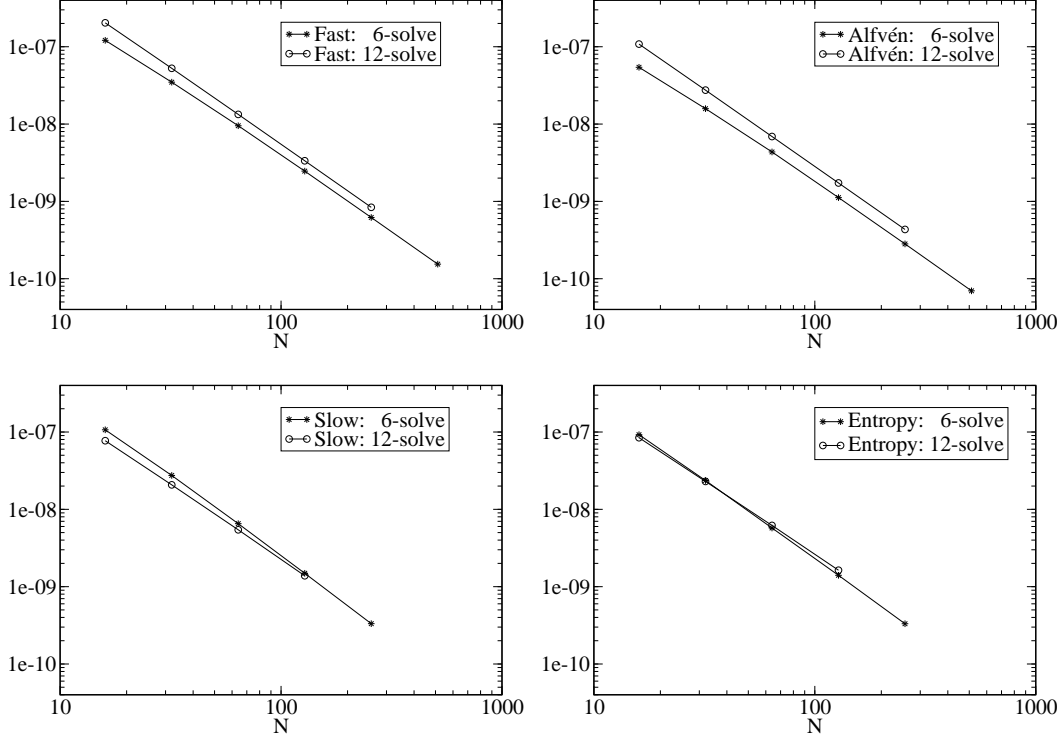
Fig. 3. Linear wave convergence of fast, Alfvén, slow and entropy modes using the CTU + CT 6-solve and 12-solve integration algorithms. The symbols denote the calculated L1-error norm.

exact nonlinear solution to the ideal MHD equations. Hence, this problem enables one to easily measure the nonlinear convergence to a multidimensional solution of the ideal MHD equations [20]. This problem is also interesting from the point of view that for a range of parameters, the circularly polarized Alfvén wave is susceptible to a parametric instability [12,10]. Unfortunately, this situation has also hindered its applicability as a general and robust test for multidimensional MHD algorithms [16,14]. For the parameters used here, and suggested by Tóth [20] we find no indication of instability.

As with the linear wave propagation study presented in §6.2, the initial conditions are most easily described in a coordinate system (x_1, x_2, x_3) which is chosen such that the wave propagates parallel to the x_1-axis. In this coordinate system, the magnetic field components $B_1 = 1$, $B_2 = 0.1\sin(2\pi x_1/\lambda)$, and $B_3 = 0.1\cos(2\pi x_1/\lambda)$. The velocity components $v_1 = (0, 1)$ for traveling or standing Alfvén waves respectively, $v_2 = 0.1\sin(2\pi x_1/\lambda)$, and $v_3 = 0.1\cos(2\pi x_1/\lambda)$. The mass density $\rho = 1$ and the gas pressure $P = 0.1$, hence $\beta = 2P/B^2 \sim 0.2$.

The computational domain used in this section is identical to that used in §6.2. In particular, we use the coordinate transformation given by equations 69 and a magnetic vector potential to initialize the magnetic fields so as to ensure $\nabla \cdot \mathbf{B} = 0$. It is worth noting that this approach will necessarily result in mag-

netic pressure perturbations as a result of truncation error in initializing the magnetic field on the grid. The parallel component B_1 is a constant, and hence rotation of this component will still result in a constant set of field components with no "pressure" variation. The perpendicular components (B_2, B_3) however, will suffer some truncation error on initialization. Since $B_\perp^2 / P = 0.1$ this truncation error in initialization will drive compressive waves. Note that with this set of initial conditions and $v_1 = 0$ the Alfvén wave will travel a distance of one wavelength λ in a time $t = 1$.

As a quantitative measure of the solution accuracy, we present in figure 4 the norm of the L1 error vector (as defined in equation 71) after propagating for a time $t = 1$ for both standing and traveling wave modes. From this figure we see that both traveling and standing circularly polarized Alfvén waves converge with second order accuracy for both integration algorithms. The traveling wave mode shows a larger error amplitude relative to the standing mode, but it is worth noting that (while not shown here) the increase is fairly uniform over the components of the error vector. The 6-solve and 12-solve algorithms show quite comparable errors for both standing and traveling wave modes. When using a CFL number of 0.4, the 12-solve and 6-solve algorithms result in nearly identical errors. Increasing the CFL number to 0.8 with the 12-solve algorithm results in a slightly reduced traveling wave error, and increased standing wave error. These results indicate that the dominant difference in the L1 error between the 6-solve and 12-solve algorithms results from the CFL dependence of the truncation error.
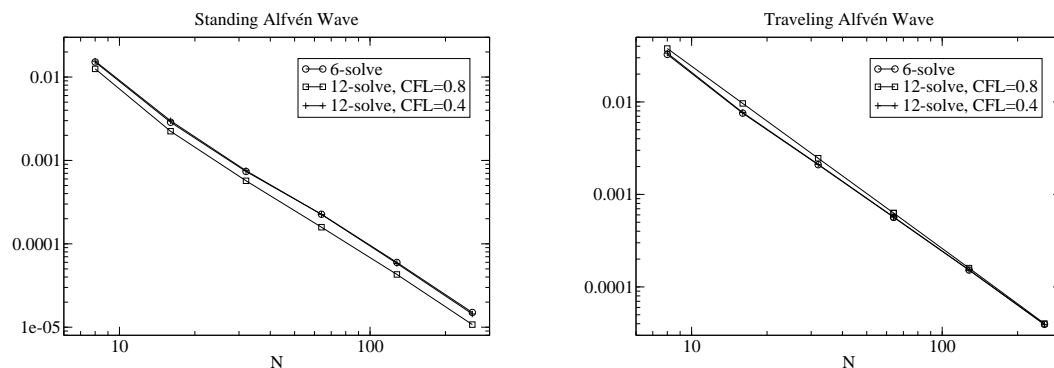

Fig. 4. L1 error norm for the 6-solve and 12-solve integration algorithms for both standing (left) and traveling (right) circularly polarized Alfvén waves. In particular note the dominant difference between the 12-solve and 6-solve errors is attributable to the CFL dependence.

As a qualitative measure of the solution accuracy, we present in figure 5 scatter plots of B_2 versus x_1 for both standing and traveling wave modes after propagating for a time $t = 5$ using the 6-solve integration algorithm. These plots are constructed using the cell center components of the magnetic field, the cell center position and the coordinate transformation given by equations 69. As a result of the fact that the wave is rotated with respect to the grid,

24

there are many grid cells with the same cell center x_1-position. Hence, since these plots include every grid point in the grid, the lack of scatter in the plots demonstrates that the Alfvén waves retain their planar symmetry throughout the calculation. Unfortunately, it is difficult to use the results presented here to make direct contact with solutions presented in the literature due to the scarcity of published three-dimensional test solutions. For analogous plots in a two-dimensional system see [20,16,1]
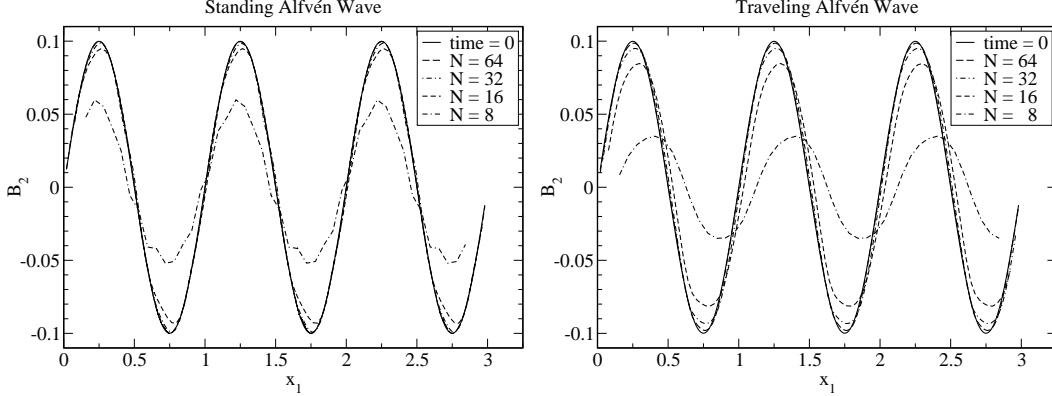

Fig. 5. Plot of B_2 versus x_1 at $t = 5$ for the standing (left) and traveling (right) circularly polarized Alfvén waves using the 6-solve integration algorithm. For comparison, the initial conditions at $t = 0$ for the $N = 64$ case is also included.

As a final measure of the solution accuracy and convergence, we present results for the dissipation of magnetic helicity in the case of a traveling circularly polarized Alfvén wave. We note that this is not the cleanest possible *test*, since with periodic boundary conditions and a mean magnetic field, it does not appear to be generally possible to define a magnetic helicity which is conserved [5]. Nevertheless, we find that following [4] the magnetic helicity evolution associated with the fluctuating components of the magnetic field gives an interesting constraint on the problem considered here. In particular, let $\mathbf{B_0} =< \mathbf{B} >$ (where angle brackets denote a spatial mean) and $\mathbf{b} = \mathbf{B} - \mathbf{B_0}$ denote the mean and fluctuating components of the magnetic field respectively. Also, define the magnetic vector potential associated with the fluctuating field as $\mathbf{b} = \nabla \times \mathbf{a}$. It is worth noting that as a result of periodic boundary conditions, $\mathbf{B_0}$ is time independent and the magnetic helicity associated with the fluctuating field $H =< \mathbf{b} \cdot \mathbf{a} >$ is gauge invariant. It follows that the time evolution of the magnetic helicity is given by

$$\frac{d}{dt} < \mathbf{b} \cdot \mathbf{a} >= -2 < \mathbf{E} \cdot \mathbf{b} > \tag{72}$$

where $\mathbf{E}$ is the electric field. Assuming ideal MHD, this equation can also be written as

$$\frac{d}{dt} < \mathbf{b} \cdot \mathbf{a} >= -2\mathbf{B_0} \cdot < \mathbf{v} \times \mathbf{b} > \ . \tag{73}$$

From this expression it is clear for a circularly polarized Alfvén wave the magnetic helicity should be conserved with $< \mathbf{b} \cdot \mathbf{a} >= B_\perp^2/k$.

In figure 6 we present the time evolution of the normalized magnetic helicity $\tilde{H} = (k/B_\perp^2) < \mathbf{b} \cdot \mathbf{a} >$ for a traveling Alfvén wave using the 6-solve integration algorithm for a variety of resolutions. The plots in this figure show two basic phenomena, dissipation and weak oscillations. The oscillations are an indication that the circularly polarized Alfvén wave is not resolved exactly. As such, certain features regarding the oscillations are worth mentioning. First, the oscillation period $\tau = 1/2$ independent of the grid resolution and whether the Alfvén wave is standing or traveling with respect to the grid. Second, the amplitude of the oscillations in the helicity varies with resolution proportional to N^{-2}. Third, the oscillations are consistent in both amplitude and phase with the independently measured volume average quantity $\mathbf{B_0} \cdot < \mathbf{v} \times \mathbf{b} >$. These details support the conclusion that the oscillations are a result of truncation error in resolving the circularly polarized Alfvén wave.
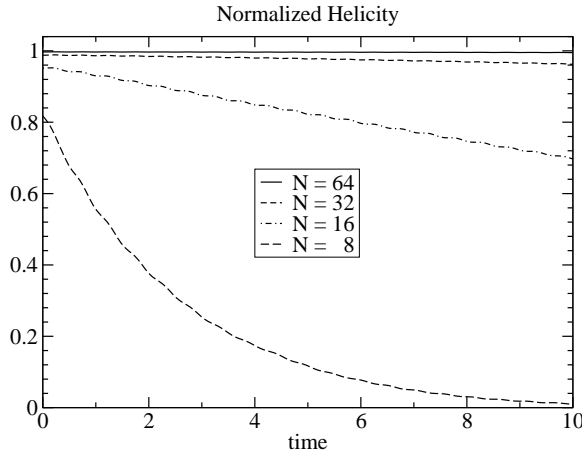

Fig. 6. Plot of the normalized magnetic helicity $\tilde{H} = (k/B_\perp^2) < \mathbf{b} \cdot \mathbf{a} >$ as a function of time for different resolutions.

6.4 MHD Riemann Problem Inclined to the Grid

In this section we present results for the solution of an MHD Riemann problem in a three dimensional domain. The Riemann problem is a favorite test problem for computational algorithms since it can be chosen to study smooth flows, discontinuous flows, or a combination thereof. Moreover, the solution to this problem can, at least in principle, be calculated exactly allowing one to verify the algorithm in some parameter regime. For multidimensional algorithms this can also be an interesting test problem when the Riemann problem interface normal direction is chosen such that it has no special orientation with respect to the computational grid. In this configuration it provides a measure of the ability of the computational algorithm to faithfully reproduce the one-

dimensional solution on the large scale, despite the fact that on the scale of grid cells the flow contains multidimensional, interacting waves. In what follows we describe the initial conditions, translation symmetry and boundary conditions for this problem and present the solution in a three-dimensional domain using the 6-solve CTU algorithm.

We begin by choosing a coordinate system (x_1, x_2, x_3) with the Riemann problem interface located at $x_1 = 0$ and will use the terms left and right states to refer to the regions $x_1 < 0$ and $x_1 > 0$ respectively. To map the initial conditions to the computational domain, we apply the coordinate transformation in equation 69 with the choice of rotation angles described below. This coordinate transformation can be inverted to read

$$
\begin{aligned}
x_1 &= x \cos \alpha \cos \beta + y \cos \alpha \sin \beta + z \sin \alpha \\
x_2 &= -x \sin \beta + y \cos \beta \\
x_3 &= -x \sin \alpha \cos \beta - y \sin \alpha \sin \beta + z \cos \alpha \ .
\end{aligned}
\tag{74}
$$

Using the fact that the initial conditions and solution to the Riemann problem are a function of the x_1-coordinate alone, the solution vector $q(\mathbf{x} + \mathbf{s}) = q(\mathbf{x})$ for a translation vector $\mathbf{s}$ which satisfies $x_1(\mathbf{x} + \mathbf{s}) = x_1(\mathbf{x})$. Making use of equation (74) we find that the continuous set of translation vectors $\mathbf{s}$, for which the solution is invariant, satisfies the equation

$$
s_x \cos \alpha \cos \beta + s_y \cos \alpha \sin \beta + s_z \sin \alpha = 0 \ .
\tag{75}
$$

Now, for the problem at hand we are interested in the discrete set of translation vectors for which $(s_x, s_y, s_z) = (n_x \delta x, n_y \delta y, n_z \delta z)$ where (n_x, n_y, n_z) are integers and $(\delta x, \delta y, \delta z)$ are the grid cell size in each direction. Making this substitution, and rearranging terms we find

$$
n_x + n_y \frac{\delta y}{\delta x} \tan \beta + n_z \frac{\delta z \tan \alpha}{\delta x \cos \beta} = 0 \ .
\tag{76}
$$

We next choose the rotation angles (α, β) such that

$$
\frac{\delta y}{\delta x} \tan \beta = \frac{r_x}{r_y} \quad \text{and} \quad \frac{\delta z \tan \alpha}{\delta x \cos \beta} = \frac{r_x}{r_z}
\tag{77}
$$

where (r_x, r_y, r_z) are integers. With this choice, our equation for translation invariance becomes

$$
\frac{n_x}{r_x} + \frac{n_y}{r_y} + \frac{n_z}{r_z} = 0 \ .
\tag{78}
$$

This is the key relation describing the discrete translation invariance of the initial conditions, and solution.

There are a couple of interesting implications of this equation which are of practical importance for this Riemann problem. First, note that the translation invariance described by equation (78) was constructed by considering a point translation symmetry and as such applies equally well to volume and interface averaged quantities. That is, there are no approximations involved in the statement that $q_{i,j,k} = q_{i+n_x,j+n_y,k+n_z}$ for (n_x, n_y, n_z) which satisfy (78). Second, note that one coordinate direction, say the x-direction, can be isolated as the principle simulation direction and the transverse directions can be made as small as (r_y, r_z). Finally, note that the translation invariance relation (78) is the key relation for mapping computational grid cells to ghost cells for imposing boundary conditions.

The specific Riemann problem we consider in this section is presented in [17] in test problem 2a. In the (x_1, x_2, x_3) coordinate system, the left state is initialized with $\rho = 1.08$, $(v_1, v_2, v_3) = (1.2, 0.01, 0.5)$, $(B_1, B_2, B_3) = (2/\sqrt{4\pi}, 3.6/\sqrt{4\pi}, 2/\sqrt{4\pi})$ and $P = 0.95$. The right state is initialized with $\rho = 1.0$, $(v_1, v_2, v_3) = (0, 0, 0)$, $(B_1, B_2, B_3) = (2/\sqrt{4\pi}, 4/\sqrt{4\pi}, 2/\sqrt{4\pi})$ and $P = 0.95$. This problem is then mapped to the 3D domain with the rotation parameters $(r_x, r_y, r_z) = (1, 2, 4)$. The computational grid has $(Nx, Ny, Nz) = (768, 8, 8)$ grid cells covering the domain $-0.75 \leq x \leq 0.75$, $0 \leq y \leq 1/64$, $0 \leq z \leq 1/64$ and hence has a resolution of $\delta x = \delta y = \delta z = 1/512$.

The solution to this Riemann problem at time $= 0.2$ is presented in figure 7 using the 6-solve CTU algorithm. These plots include the cell-center data from every grid cell using the coordinate transformation in equation (69). The first thing to note in these plots is that since $N_y > r_y$ and $N_z > r_z$ there are multiple grid cells with the same cell-center x_1-position. Therefore, the lack of scatter in these plots indicates that the algorithm retains the planar symmetry throughout the simulation. A comparison of the results presented here to the 1D solution using the underlying PPM algorithm, with the same resolution, i.e. $\delta x = 1/512$, indicates that the 3D solution has dissipation characteristics which are nearly identical to the 1D algorithm. The dominant difference between the 1D and 3D solutions is the presence of oscillations at the slow, Alfvén and fast mode discontinuities.

One question which has received a good deal of attention with this class of problem is the ability of the computational algorithm to maintain the parallel component of the magnetic field, B_1, equal to a constant. We wish to point out here that oscillations are likely unavoidable unless the orientation of the Riemann problem is chosen to be aligned in a special direction with respect to the grid. As evidence of this fact, we note that the in the initial
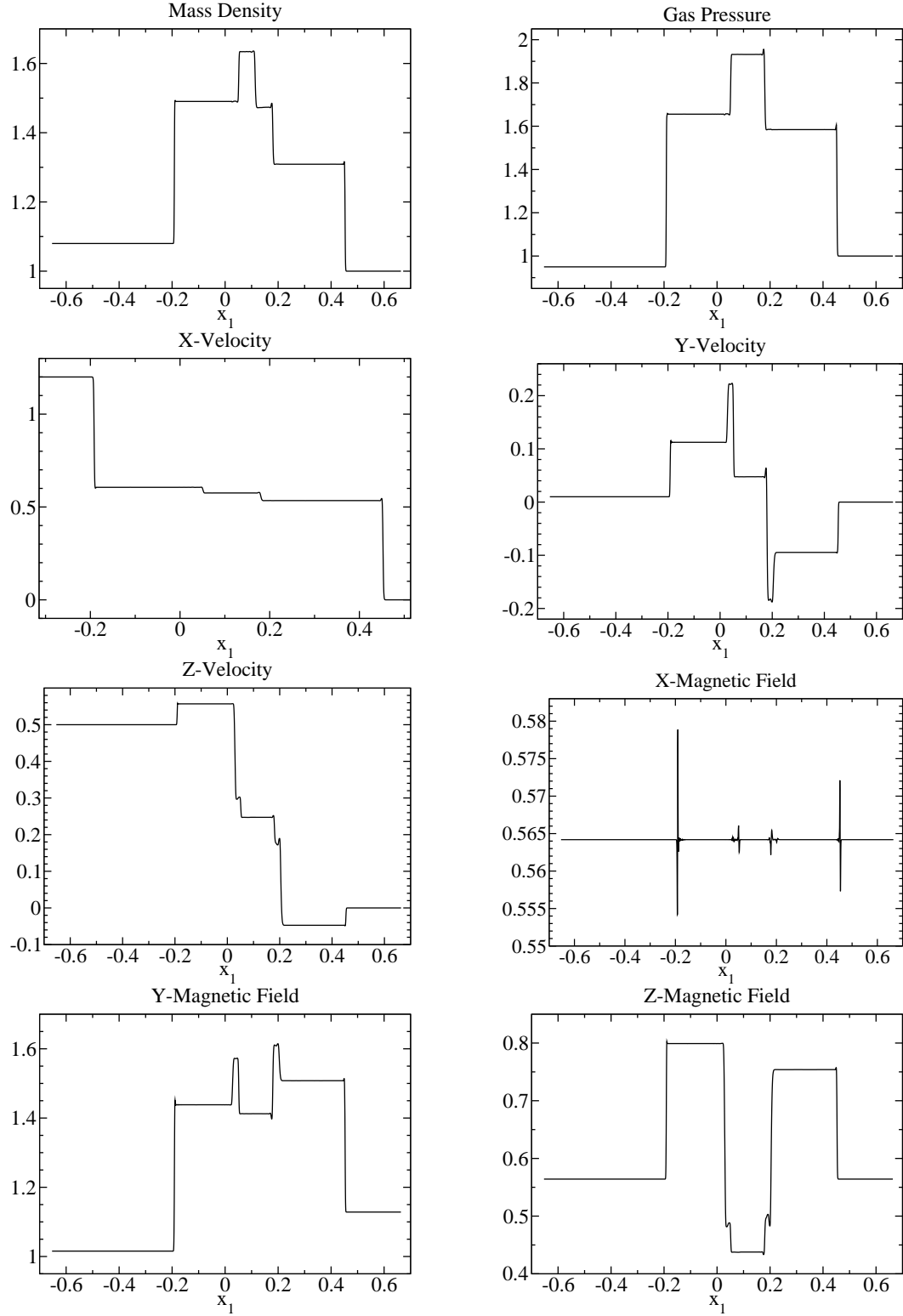
Fig. 7. Solution to the Riemann problem in a direction oblique to the grid.

conditions, the cell-center B_1-component of the magnetic field shows an oscillation with an amplitude of approximately 8.26×10^{-3} despite the fact that

the interface averaged magnetic fields were initialized with an "exact" integral average using a magnetic vector potential. This oscillation is therefore a result of the discretization relating the cell-center and interface averaged magnetic field components. In the initial conditions, as well as the solution at time $= 0.2$, the oscillations in B_1 occur wherever the transverse components of the magnetic field rotate over a small scale such as the initial discontinuity, and the resultant fast, Alfvén and slow mode discontinuities. Finally, we note that just as in the 2D paper [1], the oscillations in the parallel component of the magnetic field can be eliminated by restricting the solution to "macrocells". This operation effectively aligns the the x_1-direction with the macrocell $[1, 1, 1]$ direction.

6.5   MHD Blast Wave

Another problem which has been computed by a number of authors is the explosion of a centrally over pressurized region into a low pressure, low β ambient medium. This is an interesting problem in the sense that it combines shocked flows, smooth flow regions, and strong magnetic fields. While the results of this test are not particularly quantitative in their measure of the accuracy, this test is a good measure of the robustness of the integration algorithm. Variants on this problem have been presented by a number of authors [21,3,13,1] and here we choose to use the parameters given by [13] for a three-dimensional domain.

The computational domain extends from $-0.5 \leq x \leq 0.5$, $-0.5 \leq y \leq 0.5$ and $-0.5 \leq z \leq 0.5$. The density $\rho = 1$, the velocity $\mathbf{v} = \mathbf{0}$, and the magnetic field components $B_x = B_z = 10/\sqrt{2}$ and $B_y = 0$. Within a sphere of radius $R = 0.125$ about the origin the gas pressure $P = 100$ and $\beta = 2P/B^2 = 2$. Outside of this sphere, the gas pressure $P = 1$ and $\beta = 2 \times 10^{-2}$. These initial conditions are evolved until a time $t = 0.02$ using a 200^3 computational grid.

In figure 8 we present images of the density, pressure, magnetic and kinetic energy density sliced along the $y = 0$ plane at the end time. The general structure of the solution is the same as one finds in the 2D calculation. Namely, the outermost surface in this expanding shell is a fast-shock which is only weakly compressive and energetically is dominated by the magnetic field. Interior to this, one finds two dense shells of gas which propagate parallel to the magnetic field. These shells are bounded by a slow-mode shock and contact surface (separating the initially hot, interior gas from the surrounding cool ambient medium) on the outer and inner surfaces respectively. The maximum compression of the ambient gas by the slow-mode shock is approximately 3.3, the same as was found in the 2D calculation. The fact that the 2D and 3D calculations show quantitatively similar compression in the show-mode shock is

an indication that their motion is approximately one-dimensional, i.e. parallel to the magnetic field.

The results of this section are interesting from the point of view that they demonstrate that the 6-solve integration algorithm is a robust algorithm, capable of evolving shocked flows with $\beta \sim 10^{-2}$. Moreover, since the integration algorithm is unsplit, it preserves the symmetry of the initial conditions naturally.
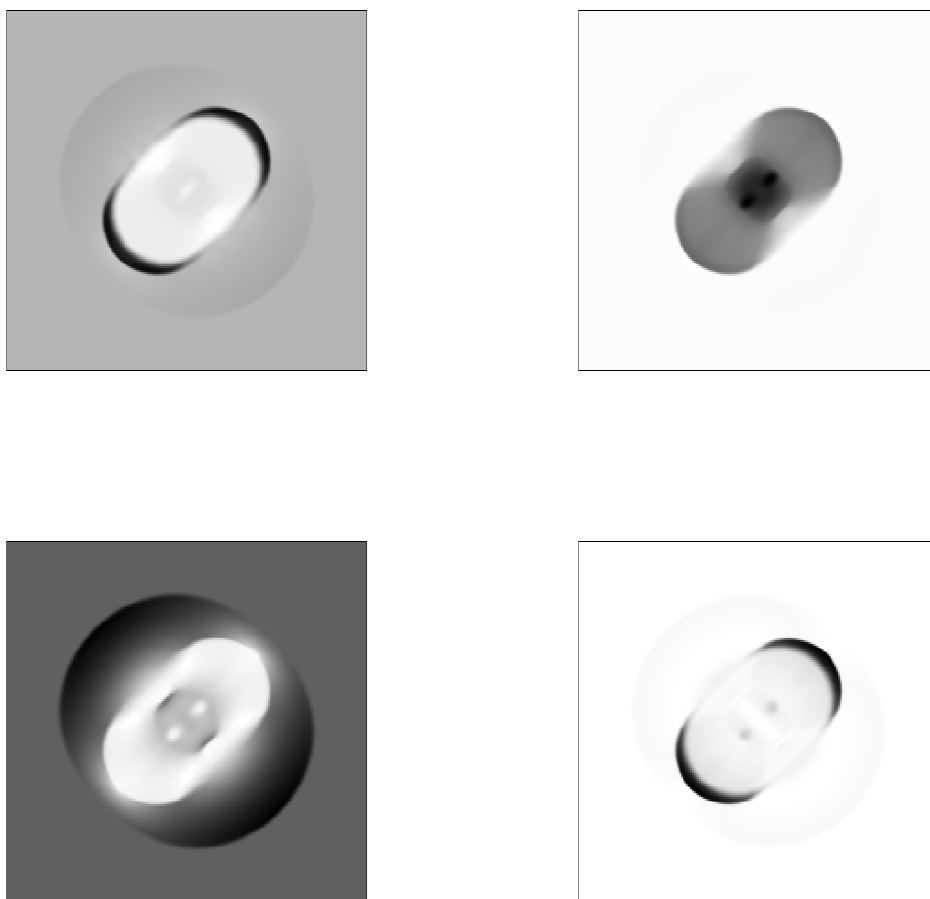

Fig. 8. Linearly scaled grey-scale images of the evolved state (time=0.02) for the MHD blast wave problem. The density (*top left*) ranges from 0.190 (white) - 2.98 (black). The gas pressure (*top right*) ranges from 1.0 (white) - 42.4 (black). The magnetic energy density (*bottom left*) ranges from 25.2 (white) - 64.9 (black). The kinetic energy density (*bottom right*) ranges from 0.0 (white) - 33.1 (black).

7   Conclusion

In this paper we have presented a three-dimensional MHD integration algorithm which combines the (6-solve) Corner Transport Upwind integration algorithm with the method of Constrained Transport for evolving the magnetic field. This integration algorithm is a natural extension, and generalization of the two-dimensional algorithm [1]. In addition we have outlined the essential elements to constructing a 12-solve CTU with CT integration algorithm for MHD and included results of this algorithm in §6. Both the 6-solve and 12-solve algorithms are found to be accurate and robust for approximately the same computational cost. As a result, we generally prefer the 6-solve algorithm as a result of its simplicity and smaller memory footprint.

The three-dimensional MHD PPM interface states algorithm presented in this paper is a new and essential element of the integration algorithms. We have shown here that this is a natural extension of the 2D MHD PPM interface states algorithm presented in [1] and that it reduces identically to the 2D algorithm in the grid-aligned, plane-parallel limit. The 3D MHD PPM interface states algorithm was designed in such a way as to satisfy a multidimensional balance law involving what we have referred to here as MHD source terms. Failure to satisfy this balance law is found to result in erroneous and secular evolution of the magnetic field under quite general conditions, e.g. the advection of a high β magnetic field loop.

We have also presented a variety of test results for both the 6- and 12-solve MHD CTU CT integration algorithms. These test problems were selected so as to enable a comparison with previously published results, as well as to introduce new, quantitative measures of the the solution accuracy. One interesting result of these tests is the observation that the dominant difference in the L1 error for the 6- and 12-solve algorithm convergence on smooth wave propagation is attributable to the CFL number dependence. Throughout this section we have included the necessary information so as to enable other researchers involved in developing or applying MHD algorithms to make a quantitative, as well as qualitative, comparison with the results in this paper.

Finally, it is worth noting that the integration algorithms presented here have been thoroughly tested on a great many test problems not included here. These include problems which are also of interest for their scientific merit. Examples include a study of the magneto-rotational instability [2] and the MHD Raleigh Taylor instability [19]. In a future paper we will detail our approach to combining the integration algorithms presented here with the methods of static and adaptive mesh refinement.

8   Acknowledgments

A   Linear Wave Right Eigenvectors

In order to enable others to perform the linear wave convergence test presented in section 6.2 and compare their results in a quantitative manner, we include the numerical values for the right eigenvectors here. In the wave-aligned coordinate system $(x_1,\ x_2,\ x_3)$ the conserved variable vector and right eigenvectors (labeled according to their propagation velocity) are given by

$$
q = \begin{pmatrix} \rho \\ \rho v_1 \\ \rho v_2 \\ \rho v_3 \\ B_1 \\ B_2 \\ B_3 \\ E \end{pmatrix}, \quad
R_{\pm c_f} = \frac{1}{2\sqrt{5}} \begin{pmatrix} 2 \\ \pm 4 \\ \mp 2 \\ 0 \\ 0 \\ 4 \\ 0 \\ 9 \end{pmatrix}, \quad
R_{\pm c_a} = \begin{pmatrix} 0 \\ 0 \\ 0 \\ \mp 1 \\ 0 \\ 0 \\ 1 \\ 0 \end{pmatrix},
$$

$$
R_{\pm c_s} = \frac{1}{2\sqrt{5}} \begin{pmatrix} 4 \\ \pm 2 \\ \pm 4 \\ 0 \\ 0 \\ -2 \\ 0 \\ 3 \end{pmatrix}, \quad
R_{v_1} = \frac{1}{2} \begin{pmatrix} 2 \\ 2 \\ 0 \\ 0 \\ 0 \\ 0 \\ 0 \\ 1 \end{pmatrix}. \tag{A.1}
$$

33

References

[1] T. A. Gardiner & J. M. Stone, An Unsplit Godunov Method for Ideal MHD via Constrained Transport, *J. Comput. Phys.* **205**, 509 (2005).

[2] Balbus, S. A. and Hawley, J. F., Instability, turbulence, and enhanced transport in accretion disks, *Rev. Mod. Phys.* **70**, 1 (1998).

[3] D. S. Balsara & D. S. Spicer, A Staggered Mesh Algorithm Using High Order Godunov Fluxes to Ensure Solenoidal Magnetic Fields in Magnetohydrodynamic Simulations, *J. Comput. Phys.* **149**, 270 (1999).

[4] A. Brandenburg & W. H. Matthaeus, Magnetic Helicity evolution in a periodic domain with imposed field, *Phys. Rev. E* **69**, 056407 (2004).

[5] M. A. Berger, Magnetic helicity in a periodic domain, *J. Geophys. Res.* **102**, 2637 (1997).

[6] J. U. Brackbill & D. C. Barnes, The Effect of Nonzero $\nabla \cdot \mathbf{B}$ on the Numerical Solution of the Magnetohydrodynamic Equations, *J. Comput. Phys.* **35**, 426 (1980).

[7] P. Colella, Multidimensional Upwind Methods for Hyperbolic Conservation Laws, *J. Comput. Phys.* **87**, 171 (1990).

[8] P. Colella & P. R. Woodward, The Piecewise Parabolic Method (PPM) for Gas-Dynamical Simulations, *J. Comput. Phys.* **54**, 174 (1984).

[9] R. K. Crockett, P. Colella, R. T. Fisher, R. I. Klein & C. F. McKee, An Unsplit, Cell-Centered Godunov Method for Ideal MHD, *J. Comput. Phys.* **203**, 422 (2005).

[10] L. Del Zanna, M. Velli, & P. Londrillo Parametric decay of circularly polarized Alfvén waves: Multidimensional simulations in periodic and open domains, *Astron. Astrophys.* **367**, 705 (2001).

[11] C. R. Evans & J. F. Hawley, Simulation of Magnetohydrodynamic Flows: A Constrained Transport Method, *Astrophys. J.* **322**, 659 (1988).

[12] M. L. Goldstein, An Instability of Finite Amplitude Circularly Polarized Alfvén Waves, *Astrophys. J.* **219**, 700 (1978).

[13] P. Londrillo & L. Del Zanna, High-Order Upwind Schemes for Multidimensional Magnetohydrodynamics *Astrophys. J.* **530**, 508 (2000).

[14] P. Londrillo & L. Del Zanna, On the divergence free condition in Godunov-type schemes for ideal magnetohydrodynamics: the upwind constrained transport algorithm *J. Comput. Phys.* **195**, 17 (2004).

[15] G. H. Miller & P. Colella, A Conservative Three-Dimensional Eulerian Method for Coupled Solid-Fluid Shock Capturing, *J. Comput. Phys.* **183**, 26 (2002).

[16] U. Pen, P. Arras, & S. Wong, A Free, Fast, Simple and Efficient TVD MHD Code, *Astrophys. J. Supp.* **149**, 447 (2003).

[17] D. Ryu & T. W. Jones, Numerical Magnetohydrodynamics in Astrophysics: Algorithm and Tests for One-Dimensional Flow, *Astrophys. J.* **442**, 228 (1995).

[18] J. Saltzman, An Unsplit 3D Upwind Method for Hyperbolic Conservation Laws, *J. Comput. Phys.* **115**, 153 (1994).

[19] J.M. Stone & T.A. Gardiner, Nonlinear Evolution of the Magnetohydrodynamic Rayleigh-Taylor Instability, *Phys. Fluids*, accepted.

[20] G. Tóth, The $\nabla \cdot \mathbf{B} = 0$ Constraint in Shock-Capturing Magnetohydrodynamics Codes, *J. Comput. Phys.* **161**, 605 (2000).

[21] A. L. Zachary, A. Malagoli & P. Colella, A Higher-Order Godunov Method for Multidimensional Ideal Magnetohydrodynamics, *SIAM J. Sci. Comp.* **15**, 263 (1994).